



# AERODYNAMIC CHARACTERISTIC AND FLOW PATTERN ON DIMPLES STRUCTURE OF A SPHERE

Katsumi Aoki<sup>1</sup>, Koji Muto<sup>2</sup>, Hiroo Okanaga<sup>3</sup> and Yasuki Nakayama<sup>4</sup>

## ABSTRACT

The fluid force on a sphere with dimples has been investigated in Reynolds number range from  $0.4 \times 10^5$  to  $1.7 \times 10^5$ . Two spheres of diameter 42.6 and 100mm were studied with 328 dimples on their surface. In the present study, the dimples in the form of three types (arc, cone and trapezoid type) were used. And more, the depth ratio of arc type dimple ( $k/d$ ) ( $k$ : the depth of dimple,  $d$ : the diameter of sphere) was changed from 0.0018 to 0.0188. The drag on a sphere with dimples was measured using a three components load cell with a strain gage. The pressure distribution around a sphere with dimples was measured using a semiconductor pressure transducer. The flow pattern around a sphere with dimples was visualized with the spark tracing method. In addition, a detailed flow pattern around a sphere with dimples was clarified by a computation according to Large Eddy Simulation (LES). From these results, the relation between the drag and the flow pattern around a sphere with dimples became clear.

**Keywords:** Sphere, Dimple structure, Drag coefficient, Flow visualization, CFD

## 1. INTRODUCTION

It is well known that the relation between the Reynolds number and the drag coefficient of a sphere have the sub critical, the critical and the super critical region. In the sub critical region, the drag coefficient shows constant value about 0.45. In the critical region, the drag coefficient decreases suddenly and reaches a minimum value. In the super critical region, the drag coefficient gradually increases after suddenly decrease. The critical region is the transition region from laminar flow to turbulence flow, it influences both the drag and the lift significantly and the flow pattern around a sphere in this region becomes complex. Also, it is known that the critical region is influenced by the surface structures which are the roughness and the dimple etc. The turbulence transition on flow is promoted by these surface structures, as a result, the critical region shifts to the lower Reynolds number<sup>(1)</sup>. If an optimum surface structure for reducing the drag is clarified, the flow resistance will be able to be controlled effectively. However, the relation between the drag and the flow pattern around a sphere with surface structures has

---

<sup>1</sup> Corresponding author: Professor, Department of Mechanical Engineering, Tokai University, Japan,  
e-mail: [katumi@keyaki.cc.u-tokai.ac.jp](mailto:katumi@keyaki.cc.u-tokai.ac.jp)

<sup>2</sup> Graduate student, Course of Mechanical Engineering, Tokai University, Japan

<sup>3</sup> Associate professor, Department of Mechanical Engineering, Tokai University, Japan,

<sup>4</sup> Future Technology Research Institute

many uncertainly part because the flow around a sphere with surface structures is complex. So far, the reports on flow past a sphere with surface structures were focusing on the aerodynamic characteristics of a golf ball. For example, Bearman and Harvey<sup>(2)</sup>, Smits and Smith<sup>(3)</sup> have reported the studies about the drag and the lift characteristics of a golf ball and the spin rate decay. Ting<sup>(4)</sup> studied the effects of dimple width and depth on the aerodynamic characteristics for a golf ball by CFD. Aoki<sup>(5)</sup> studied the effects of dimple number, depth and shape on the aerodynamic characteristics for a golf ball by some experiments and CFD. However, it is difficult to clarify the flow pattern around a golf ball because the flow pattern complying with the dimple structure on its surface is so complicated. The final purpose of this study is to clarify the optimum surface structure of a sphere. So, this paper describes the relation between the drag and the flow pattern around a sphere with dimples. In the present study, the dimples in the form of three types (arc, cone and trapezoid type) were used. And more, the depth ratio of arc type dimple ( $k/d$ ) ( $k$ : the depth of dimple,  $d$ : the diameter of sphere) was changed from 0.0018 to 0.0188. The drag, the pressure distribution and the flow pattern around a sphere with dimples were studied experimentally. In addition, a detailed flow pattern around a sphere with dimples was clarified by a computation according to Large Eddy Simulation (LES). From these results, the relation between the drag and the flow pattern around a sphere with dimples became clear.

## 2. EXPERIMENTAL APPARATUS AND METHOD

### 2.1. Test spheres

The test spheres are made of vinyl chloride and these are 42.6 and 100mm in diameter ( $d$ ). Figure 1 shows the dimples in section. In the present study, the dimples in the form of three types (arc, cone and trapezoid type) were used. And more, the depth ratio of arc type dimple ( $k/d$ ) ( $k$ : the depth of dimple) was changed from 0.0018 to 0.0188. The width ratio of dimple ( $c/d$ ) ( $c$ : the width of dimple) is constant value at 0.0828. A total of 328 dimples are distributed uniformly over the test sphere. Then, there is a pressure hole on the test sphere surface ( $d=100\text{mm}$ ) which is 0.8mm in diameter. Two spheres (the one has a pressure hole in the inside of dimple and another one has it in the outside of dimple) were used in the pressure measurement. Table 1 shows the main specifications of the test sphere.

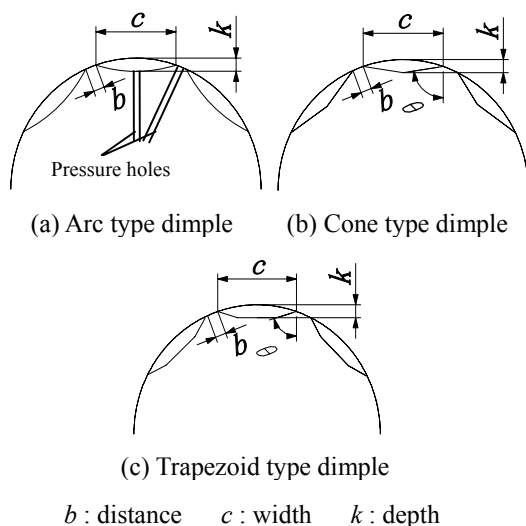


**Fig.1. Sectional views of dimple**

**Table 1. Specifications of test sphere surface**

Type	Shape of dimple	$b/d$	$c/d$	$k/d$	$k/c$
Smooth	-	-	-	-	-
A	Arc	0.0152	0.0828	0.0018	0.0211
B				0.0025	0.0302
C				0.0030	0.0362
D				0.0047	0.0573
E				0.0079	0.0958
F				0.0112	0.1350
G				0.0151	0.1830
H				0.0188	0.2270
I	Cone			0.0079	0.0958
J	Trapezoid			0.0079	0.0958

## 2.2. Measurement of drag and pressure

The blow-down type wind tunnel of test-section size 400×400mm is used for aerodynamic measurements and flow visualization of the test sphere. The free stream velocity ( $U$ ) is varied from 15 to 60m/s. And, the turbulence intensity in this velocity range is 0.3%. The Reynolds number ( $Re=Ud/\nu$ ,  $\nu$ : the kinematic viscosity) based on the free stream velocity and the sphere diameter is from  $0.4\times 10^5$  to  $1.7\times 10^5$ . In the experiments, the dimples in the form of arc type dimple (TypeE, TypeG and TypeH) were used. Figure 2 (a) shows the outline of measurement equipment for the drag ( $D$ ). The size of the frame is 500×500mm which is placed at 100mm from the outlet of the wind tunnel. The test sphere ( $d=42.6$ mm) is fixed at the center of the frame using a piano wire, giving a tension at both fixed ends. The drag on the test sphere is measured by a three components load cell with a strain gage attached below the frame. Then, the measured drag is included not only the drag of the test sphere but also that of the piano wire because the test sphere and the piano wire are united. So, the drag of the piano wire is expected from the measured drag. From this drag value, the drag coefficient ( $C_D$ ) is calculated by equation (1). Figure 2 (b) shows the outline of measurement equipment for the pressure ( $P$ ). The test sphere ( $d=100$ mm) is placed at 100mm from the outlet of the wind tunnel by a hollow shaft including a small pipe. It is shown in figure 1, there is a pressure hole on the test sphere surface which are 0.8mm in diameter. Two spheres (the one has a pressure hole in the inside of dimple and another one has it in the outside of dimple) were used in the pressure measurement. The one side of the small pipe is connected with the pressure hole at the center of the test sphere and another side of the small pipe connected with a semiconductor pressure transducer. The pressure distribution over the test sphere surface is measured using the semiconductor pressure transducer at every  $\theta=3^\circ$  in the angular range from  $0^\circ$  (the stagnation point) to  $180^\circ$ . From this pressure value, the pressure coefficient ( $C_P$ ) is calculated by equation (2).

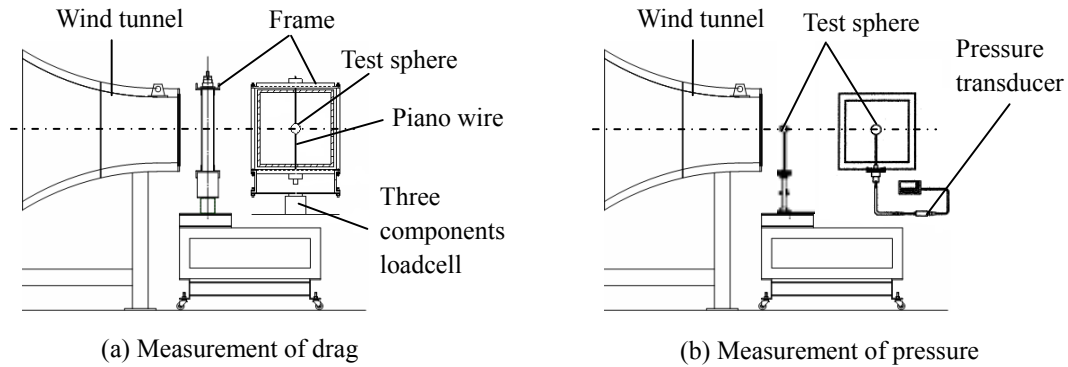


**Fig.2. Outlines of measurement equipment**

$$C_D = \frac{2D}{A\rho U^2} \quad (1)$$

$$C_P = \frac{P - P_0}{\rho U^2 / 2} \quad (2)$$

$D$  : Drag of sphere [N]

$\rho$  : Density of air [ $\text{kg}/\text{m}^3$ ]

$P$  : Pressure of sphere surface [Pa]

$A$  : Projected area [ $\text{m}^2$ ]

$U$  : Free stream velocity [m/s]

$P_0$  : Pressure of free stream velocity [Pa]

## 2.3. Flow visualization

Figure 3 shows the schematic view of measurement equipment for the spark tracing method. Two needle electrodes are set on the test sphere surface at  $\theta=\pm 60^\circ$  and two line electrodes set 30mm away from the test sphere. The high voltage and high frequency pulses are supplied from a pulse generator.

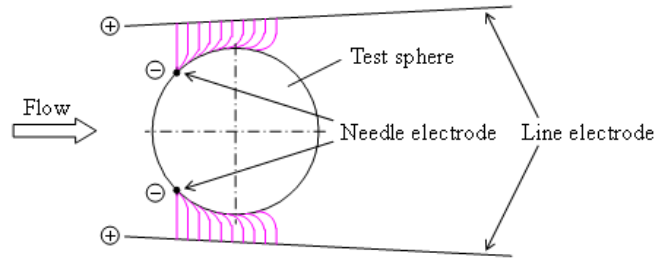


**Fig.3. Outline of measurement equipment for spark tracing method**

### 3. COMPUTER FLUID DYNAMICS (CFD)

The general-purpose thermal fluid analysis software (FLUENT) according to Large Eddy Simulation (LES) is used for the computation. Figure 4 shows the layout of analysis domain. It makes non-structural triangular meshes at the test sphere surface and non-structural tetrahedron mesh in the other spaces. There are about one million meshes in the analysis domain. The test sphere is 42.6mm in diameter ( $d$ ). The size of analysis domain is  $1278 (30d)^L \times 639 (15d)^W \times 639 (15d)^H$  mm and the test sphere is placed at  $426 (10d)$  mm from the inlet section. And, the Reynolds number ( $Re$ ) based on the free stream velocity and the sphere diameter is  $Re=1.27 \times 10^5$ . Table 2 shows the boundary conditions.

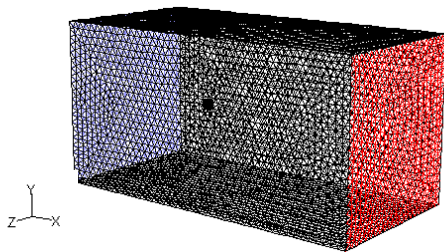


**Fig.4. Analysis domain**

**Table 2. Boundary conditions**

Software	FLUENT6.2	
Model	LES (Smagorinsky-Lilly : $C_s=0.1$ )	
Grid system	Unstructured mesh (Triangle mesh)	
Cells	About 1,000,000	
Calculation condition	Unsteady	
	Time step	0.001 [s]
	Iteration time	1000
Input condition	Inflow	Velocity inlet : 45 [m/s]
	Outflow	Pressure outlet : 0 [Pa]
Analytical area	Size of the flow box	$1278(30d) \times 639(15d) \times 639(15d)$ [mm]
	Sphere position	426(10d) [mm]

## 4. RESULTS AND CONSIDERATIONS

### 4.1. Drag coefficient

Figure 5 shows the drag coefficient ( $C_D$ ) variation with the Reynolds number ( $Re$ ). However, the computational  $C_D$  are only in case of  $Re=1.27 \times 10^5$ . It is seen that  $C_D$  of the smooth sphere is constant value at about  $C_D=0.45$  for the change of  $Re$  and in the sub critical region. On the other hand,  $C_D$  of TypeE shows significant variation with  $Re$ . The change over from the sub critical region to the critical region is taking place around  $Re=0.5 \times 10^5$ . At this  $Re$ ,  $C_D$  drops suddenly to about  $C_D=0.25$ . By giving the dimple on the sphere surface, the critical region of the sphere with dimples shifts to the lower  $Re$  side

compared to that of the smooth sphere. Furthermore, as the depth of dimple becomes deeper, the critical region shifts to the lower  $Re$  side and  $C_D$  in the super critical region becomes larger. Here, as the depth of dimple becomes deeper, the computational  $C_D$  becomes larger also. Form these results, the tendency of the computational  $C_D$  agrees with the experimental  $C_D$ . Figure 6 shows the experimental and the computational  $C_D$  variation with the depth ratio of dimple ( $k/d$ ) in case of  $Re=1.27\times 10^5$ . The point of  $k/d=0$  indicates for the smooth sphere. From these results, it is seen that  $C_D$  decreases as  $k/d$  increases from  $k/d=0$ . Then,  $C_D$  becomes a minimum value at  $k/d=0.003$ . As  $k/d$  increases from  $k/d=0.003$ ,  $C_D$  increases again. Furthermore,  $C_D$  by the shape of dimple increases in order of cone, arc ( $k/d=0.0079$ ) and trapezoid type dimple.

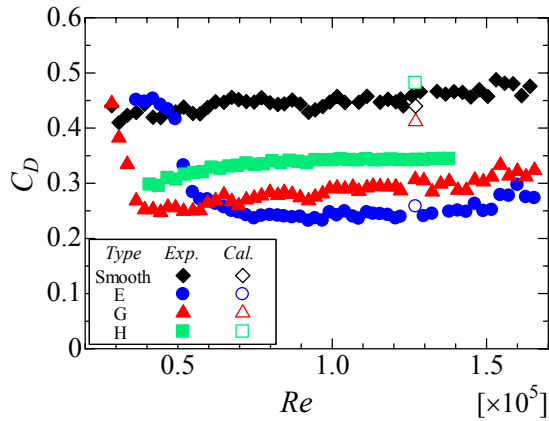


Fig.5. Drag coefficient for Reynolds number

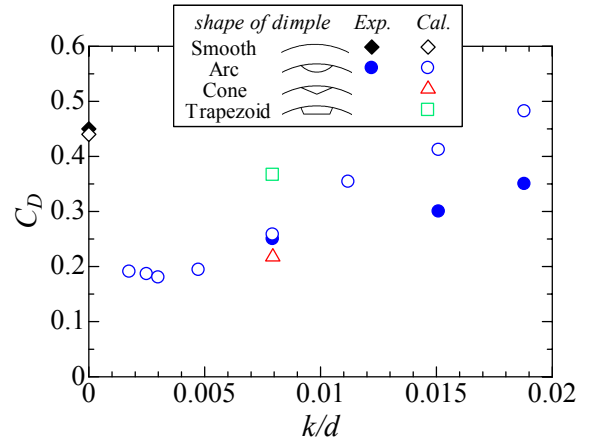


Fig.6. Drag coefficient for  $k/d$

## 4.2. Pressure coefficient distribution

### 4.2.1. Depth of dimple

Figure 7 shows the pressure coefficient ( $C_p$ ) distributions by the depth of dimple in case of  $Re=1.27\times 10^5$ . Here,  $\theta$  shows the angle measured from the stagnation point ( $\theta=0^\circ$ ) and  $C_p$  of the sphere with dimples shows the average  $C_p$  of the inside and the outside of dimple. Figure 7 (a) shows the experimental and computational  $C_p$  distributions.  $C_p$  of the smooth sphere shows the minimum value at the vicinity of  $\theta=72^\circ$ , and after reaching the minimum value,  $C_p$  begins to show constant value at the vicinity of  $\theta=80^\circ$ . From this result, it is thought that the separation point is the vicinity of  $\theta=80^\circ$ . On the other hand,  $C_p$  of TypeE shows the minimum value at the vicinity of  $\theta=90^\circ$ , and after reaching the minimum value,  $C_p$  begins to show constant value beyond  $\theta=120^\circ$ . From these results, it is seen that the velocity around TypeE is faster than that around the smooth sphere. Also, the separation point of TypeE shifts to the downstream side compared with that of smooth sphere and the back pressure coefficient of TypeE is larger than that of the smooth sphere. This clearly shows, as seen from figure 5,  $C_D$  of TypeE is smaller than that of the smooth sphere. Furthermore,  $C_p$  of TypeH is the minimum value at the vicinity of  $\theta=80^\circ$ , and becomes constant value beyond  $\theta=110^\circ$ . Thus, as the depth of dimple becomes deeper, the separation point shifts to the upstream side and the back pressure coefficient becomes smaller. This clearly shows, as seen from figure5,  $C_D$  of TypeH is larger than that of TypeE. Here, the tendency of the computational  $C_p$  agrees with the experimental  $C_p$ . Figure 7 (b) shows the computational  $C_p$  distributions only. For TypeC ( $k/d=0.003$ ) with the minimum  $C_D$  value, the separation point shifts to further downstream side and the back pressure coefficient is larger than any other spheres. As the depth of dimple becomes deeper beyond  $k/d=0.003$ , the separation point shifts to the upstream side and the back pressure coefficient becomes smaller. Then, as the depth of dimple becomes shallower below  $k/d=0.003$  (the

surface structure becomes the smooth surface), the separation point shifts to the upstream side and the back pressure coefficient becomes smaller.

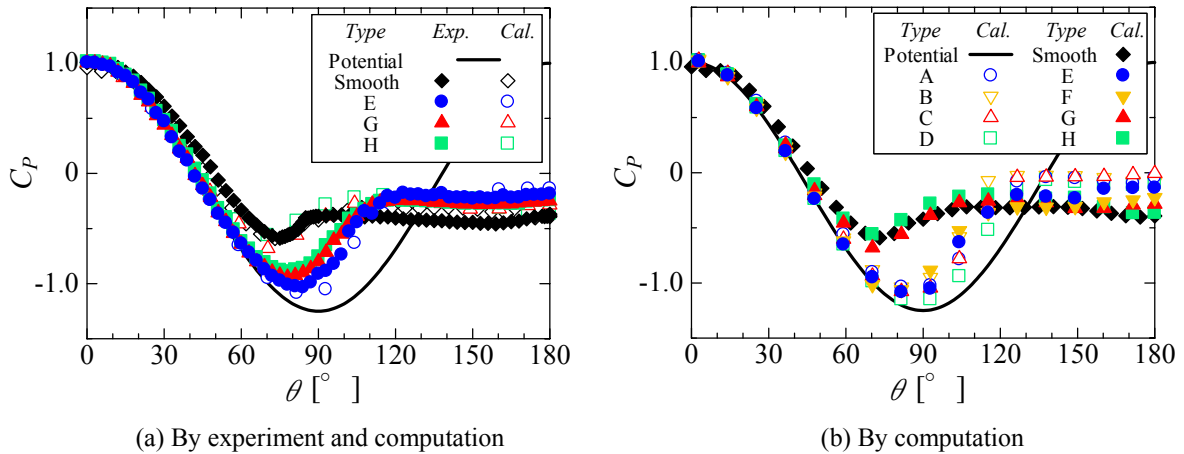


**Fig.7. Pressure coefficient distributions by depth of dimple**

#### 4.2.2. Shape of dimple

Figure 8 shows the experimental and the computational  $C_p$  distributions by the shape of dimple in case of  $Re=1.27 \times 10^5$ . Here,  $\theta$  shows the angle measured from the stagnation point ( $\theta=0^\circ$ ) and  $C_p$  of the sphere with dimples shows the average  $C_p$  of the inside and the outside of dimple. The separation point by the shape of dimple shifts to the upstream side and the back pressure coefficient by the shape of dimple becomes smaller in order of cone, arc ( $k/d=0.0079$ ) and trapezoid type dimple.

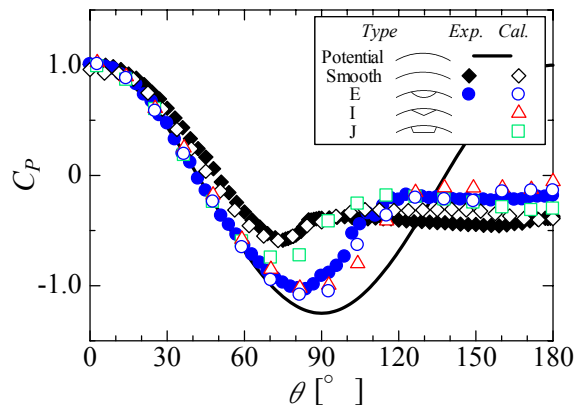


**Fig.8. Pressure coefficient distribution by shape of dimple**

#### 4.3. Flow visualization

Figure 9 shows the flow visualization around the spheres by the spark tracing method in case of  $Re=1.27 \times 10^5$ . For the smooth sphere, the separation point is the vicinity of  $\theta=80^\circ$  and the wake region is large. On the other hand, the separation point of the sphere with dimples shifts to the downstream side compared with that of smooth sphere and the wake region of the sphere with dimples is smaller than that of the smooth sphere. Furthermore, as the depth of dimple becomes deeper, the separation point shifts to the upstream side and the wake region becomes larger. Also, figure 9 shows the contours of the computational pressure coefficient distribution by the computation. The back pressure coefficient of the

smooth sphere shows constant value at the vicinity of  $\theta=80^\circ$ . On the other hand, the back pressure coefficient of the sphere with dimples shows constant value beyond  $\theta=80^\circ$ . As the depth of dimple becomes deeper, the separation point shifts to the upstream side. The separation point in the pressure coefficient distribution shows same tendency with the visualized result.

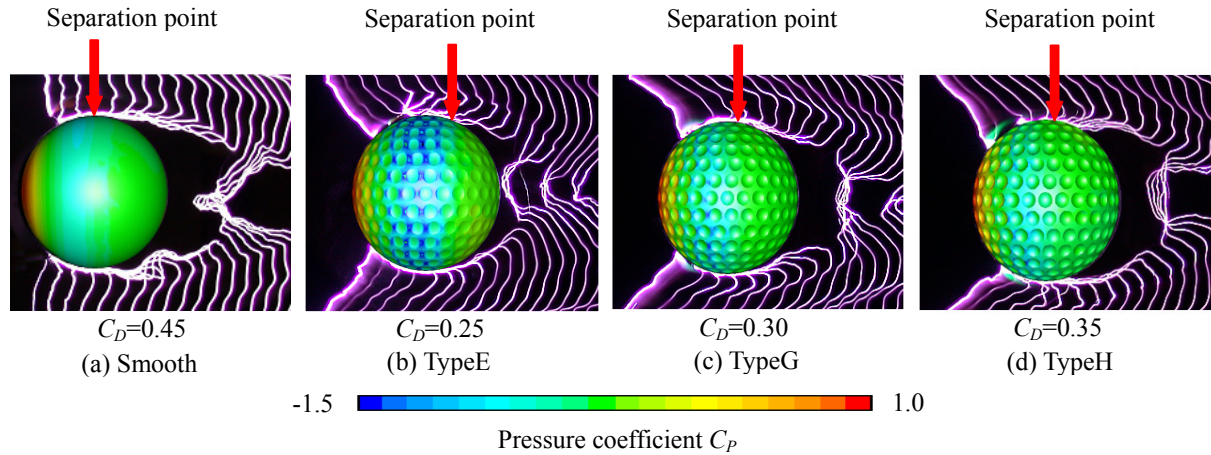


**Fig.9. Flow visualization around spheres by spark tracing method and contours of pressure coefficient distribution by computation**

#### 4.4. Velocity vector

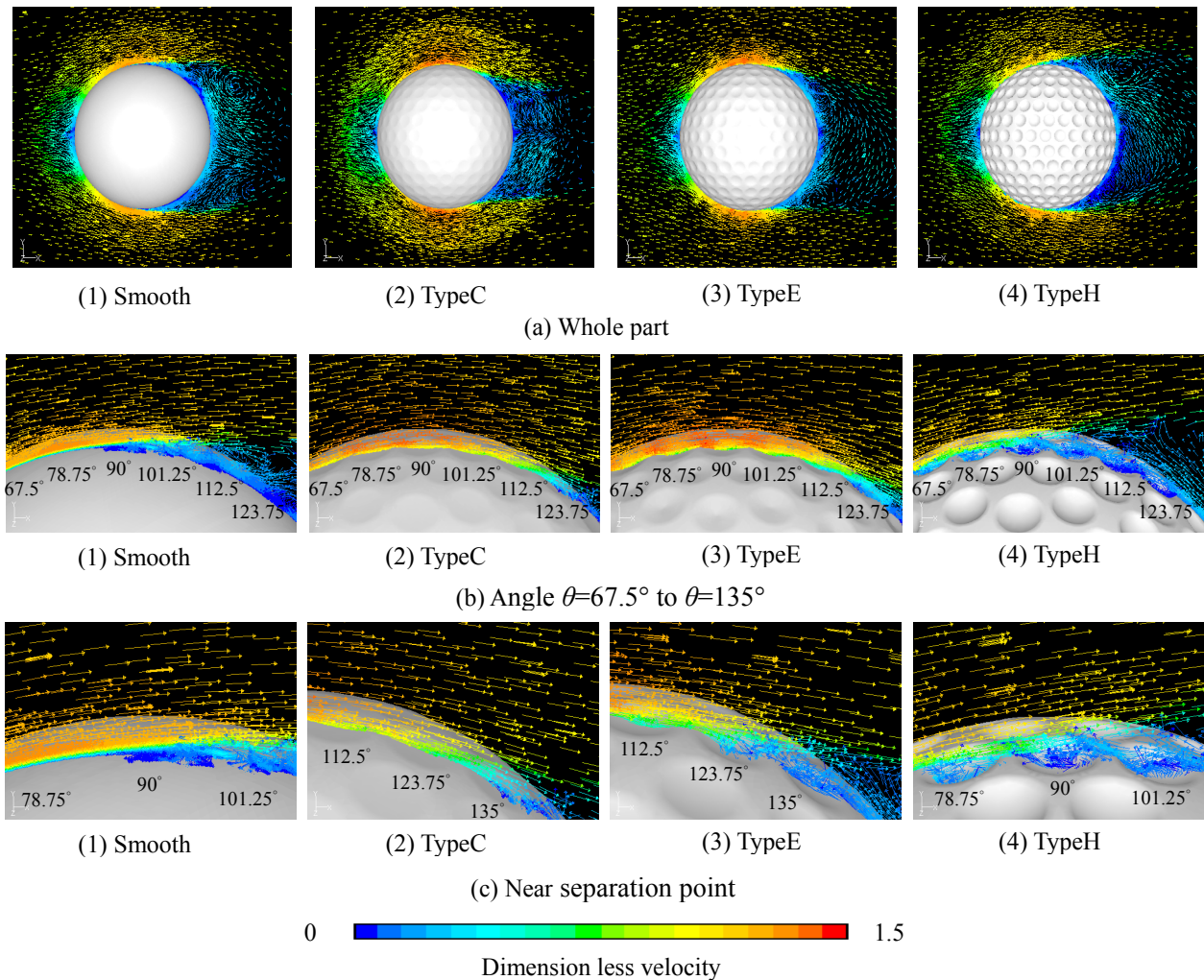
##### 4.4.1. Depth of dimple

Figure 10 shows the velocity vector (X-Y plane) around the spheres by the computation in case of  $Re=1.27 \times 10^5$ . Here, the velocity range shows the dimension less value that the velocity around the sphere divided the free stream velocity. Figure 10 (a) shows the velocity vector around the spheres in whole part. The flow in the vicinity of the stagnation point is extremely slow. Then, the flow in the downstream direction is gradually accelerated. After the flow separates, the velocity is gradually decelerated to be accompanied with the reverse flow in the wake region. For the smooth sphere, the separation point is the vicinity of  $\theta=80^\circ$  and the wake region is large. On the other hand, the separation point of the sphere with dimples shifts to the downstream side compared with that of smooth sphere and the wake region of the sphere with dimples is smaller than that of the smooth sphere. For TypeC ( $k/d=0.003$ ) with the minimum  $C_D$  value, the separation point shifts to further downstream side and the wake region is smaller than any other spheres. Figure 10 (b) shows velocity vector around the spheres in the angle  $\theta=67.5^\circ$  to  $\theta=135^\circ$ . The velocity in the inside of dimple is slower than that in the outside of dimple. The flow reverses in the inside of dimple near the separation point. As the depth of dimple becomes deeper, the reversed flow in the inside of dimple appears further upstream side. On the other hand, the velocity around the shallow dimple is faster than that around the deep dimple in the same angle. Figure 10 (c) shows velocity vector around the spheres near the separation point. It is seen that the flow separates at the outside of dimple of all spheres.

##### 4.4.2. Shape of dimple

Figure 11 shows the velocity vector (X-Y plane) around the spheres by the computation in case of  $Re=1.27 \times 10^5$ . Here, the velocity range shows the dimension less value that the velocity around the sphere divided the free stream velocity. Figure 11 (a) shows the velocity vector around the spheres in whole part. The separation point by the shape of dimple shifts to the upstream side and the wake region by the shape of dimple becomes larger in order of cone, arc ( $k/d=0.0079$ ) and trapezoid type dimple. Figure 11 (b)

shows velocity vector around the spheres in the angle  $\theta=67.5^\circ$  to  $\theta=135^\circ$ . The velocity in the inside of dimple is slower than that in the outside of dimple. The flow reverses in the inside of dimple near the separation point. The reversed flow in the inside of dimple appears further upstream side in order of cone, arc ( $k/d=0.0079$ ) and trapezoid type dimple. The velocity around the cone type dimple is faster than that around the trapezoid type dimple in the same angle. Figure 11 (c) shows velocity vector around the spheres near the separation point. It is seen that the flow separates at the outside of dimple of all spheres.



**Fig.10. Velocity vector around spheres by depth of dimple**

#### 4.5. Separation point

Figure 12 shows the position of the separation point ( $\theta_s$ ) obtained from the pressure coefficient distribution and the flow visualization in case of  $Re=1.27 \times 10^5$ . Here,  $\theta_s$  shows the angle measured from the stagnation point ( $\theta=0^\circ$ ).  $\theta_s$  of smooth sphere is the vicinity of  $\theta_s=80^\circ$ . On the other hand,  $\theta_s$  of the sphere with dimples shifts to the downstream side compared with that of smooth sphere. Then, as the depth of dimple becomes deeper,  $\theta_s$  shifts to the upstream side. Furthermore,  $\theta_s$  by the shape of dimple shifts to the upstream side in order of cone, arc ( $k/d=0.0079$ ) and trapezoid type dimple. Also, figure 12 shows the computational drag coefficient ( $C_D$ ). This clearly shows, as  $C_D$  becomes larger,  $\theta_s$  shifts to the upstream side.



## 5. CONCLUSIONS

By investigating the relation between the drag and the flow pattern on the dimple structure (depth and shape of dimple) of a sphere from the experiments and the computation, the following conclusions were obtained.

- (1) The critical region of a sphere with dimples shifts to the lower Reynolds number side compared to that of a smooth sphere. Then, the depth of dimple becomes deeper, the critical region shifts to the lower Reynolds number side.
- (2) In the super critical region, the drag coefficient by the depth of dimple becomes a minimum value at the depth ratio of dimple  $k/d=0.003$ .
- (3) In the super critical region, the drag coefficient by the shape of dimple becomes larger in order of cone, arc and trapezoid type dimple.
- (4) As the depth of dimple becomes shallower below the depth ratio of dimple  $k/d=0.003$  or deeper beyond  $k/d=0.003$  in the super critical region, the separation point shifts to the upstream side and the back pressure coefficient becomes smaller.
- (5) The separation point shifts to the upstream side and the back pressure coefficient becomes smaller in order of cone, arc and trapezoid type dimple.
- (6) The flow visualization demonstrates that the separation point of a sphere with dimples shifts to the downstream side compared to that of a smooth sphere. Also, as the depth of dimple becomes deeper in the super critical region, the separation point shifts to the upstream side and the wake region becomes larger.

## REFERENCES

- (1) K. Aoki, A. Ohike, K. Yamaguchi & Y. Nakayama, Flying Characteristics and Flow Pattern of a Sphere with Dimples, *Journal of Visualization*, Vol. 6, No. 1 (2003).
- (2) P. W. Bearman & J. K. Harvey, Golf Ball Aerodynamics, *Aeronautical Quarterly* 27 (1976), pp. 112-122.
- (3) A. J. Smits. & D. R. Smith, A new aerodynamics model of a golfball in flight, *Science and Golf II* (1994), pp. 340-347.
- (4) L. L. Ting, Effects of Dimple size and depth on Golf ball Aerodynamic performance, 4th ASME - JSME Joint Fluids Engineering Conference (2004), pp. 1-7.
- (5) K. Aoki, M. Nonaka & T. Goto, Aerodynamic and Flying Characteristics for the Surface Structure on the Golf Ball, *Proceedings of the school of Engineering Tokai University*, Vol. 44, No. 2, (2004), pp. 67-72.